

# Modeling multi-fraction coastal aeolian sediment transport with horizontal and vertical grain size variability

Christa van IJzendoorn<sup>1</sup>, Caroline Hallin<sup>1</sup>, Reniers Ad<sup>1</sup>, and Sierd de Vries<sup>1</sup>

<sup>1</sup>Delft University of Technology

March 16, 2023

## Abstract

Grain size affects the rates of aeolian sediment transport on beaches. Sediment in coastal environments typically consists of multiple grain size fractions and exhibits spatiotemporal variations. Still, conceptual and numerical aeolian transport models are simplified and often only include a single fraction that is constant over the model domain. It is unclear to what extent this simplification is valid and if the inclusion of multi-fraction transport and spatial grain size variations affects aeolian sediment transport simulations and predictions of coastal dune development. This study applies the numerical aeolian sediment transport model AeLiS to compare single-fraction to multi-fraction approaches for a range of grain size distributions and spatial grain size scenarios. The results show that on timescales of days to years, single-fraction simulations with the median grain size, D50, often give similar results to multi-fraction simulations provided the wind is able to mobilize all fractions within that time frame. On these timescales, vertical variability in grain size has a limited effect on total transport rates, but it does influence the simulation results on minute timescales. Horizontal grain size variability influences both the total transport rates and the downwind bed grain size composition. The results provide new insights into the influence of beach sediment composition and spatial variability on total transport rates towards the dunes. The findings of this study can guide the implementation of grain size variability in numerical aeolian sediment transport models.

## Hosted file

958042\_0\_art\_file\_10775814\_rr5xhh.docx available at <https://authorea.com/users/595693/articles/629536-modeling-multi-fraction-coastal-aeolian-sediment-transport-with-horizontal-and-vertical-grain-size-variability>

# 1 **Modeling multi-fraction coastal aeolian sediment transport with horizontal and** 2 **vertical grain size variability**

3 C.O. van IJendoorn<sup>a</sup>, C. Hallin<sup>a, b</sup>, A.J.H.M. Reniers<sup>a</sup>, S. de Vries<sup>a</sup>

4 a) Department of Hydraulic Engineering, Delft University of Technology, Delft, the Netherlands

5 b) Lund University

## 6 **Key points**

- 7 - The effect of multi-fraction transport and spatial grain size variations were examined with the  
8 numerical aeolian transport model AeoliS.
- 9 - The  $D_{50}$  can be used as a representative grain size in aeolian sediment transport modeling on a  
10 time scale of days to years.
- 11 - The bed surface grain size in the upwind, source area might be the most relevant to include in  
12 aeolian sediment transport models.

## 13 **Abstract**

14 Grain size affects the rates of aeolian sediment transport on beaches. Sediment in coastal environments  
15 typically consists of multiple grain size fractions and exhibits spatiotemporal variations. Still, conceptual  
16 and numerical aeolian transport models are simplified and often only include a single fraction that is  
17 constant over the model domain. It is unclear to what extent this simplification is valid and if the  
18 inclusion of multi-fraction transport and spatial grain size variations affects aeolian sediment transport  
19 simulations and predictions of coastal dune development. This study applies the numerical aeolian  
20 sediment transport model AeoliS to compare single-fraction to multi-fraction approaches for a range of  
21 grain size distributions and spatial grain size scenarios. The results show that on timescales of days to  
22 years, single-fraction simulations with the median grain size,  $D_{50}$ , often give similar results to multi-  
23 fraction simulations provided the wind is able to mobilize all fractions within that time frame. On these  
24 timescales, vertical variability in grain size has a limited effect on total transport rates, but it does  
25 influence the simulation results on minute timescales. Horizontal grain size variability influences both  
26 the total transport rates and the downwind bed grain size composition. The results provide new insights  
27 into the influence of beach sediment composition and spatial variability on total transport rates towards  
28 the dunes. The findings of this study can guide the implementation of grain size variability in numerical  
29 aeolian sediment transport models.

## 30 **Plain language summary**

31 The growth of coastal dunes is caused by the wind, which moves sand from the beach to the dunes. The  
32 sand grains on the beach have different sizes. For instance, the size of the sand grains can vary from the  
33 waterline to the start of the dunes. Small sand grains are more easily picked up by the wind than larger,  
34 heavier grains. Thus, the size of sand grains and how they are spread over the beach can impact how  
35 much sand is moved by the wind. We use computer simulations to calculate how much sand is moved  
36 by the wind during different conditions. We investigate how different assumptions about the grain size  
37 on the beach influence these calculations. The results show that the calculations with one single sand  
38 size, in most cases, give comparable results to simulations with more complicated sand size variations.  
39 The simplified approach is beneficial because it reduces the need for detailed field data of grain sizes for  
40 future calculations.

## 41 **Index terms and keywords**

42 4217 Coastal processes

43 4546 Nearshore processes

44 4558 Sediment transport

45 0545 Modeling

46 Key words: grain size, aeolian processes, AeoliS, beaches

## 47 **1. Introduction**

48 Sediment available for aeolian transport in coastal settings is characterized by a grain size distribution  
49 that is typically described with a range of grain size fractions (Krumbein, 1934). Grain size affects aeolian  
50 sediment transport due to the larger drag and lift force that is necessary to displace coarser grains  
51 (Durán et al., 2011; Sarre, 1987). Grain size also alters the creep and saltation trajectory of sediment  
52 (e.g., Cheng et al., 2015; Zhang et al., 2021). Therefore, different grain size fractions lead to different  
53 rates of sediment transport.

54 Field measurements on beaches have shown considerable spatial variations in grain size in the  
55 alongshore (Hallin, et al., 2019a), cross-shore (Bauer, 1991; Çelikoğlu et al., 2006; Edwards, 2001; Sonu,  
56 1972; Stauble & Cialone, 1997; van der Wal, 2000a; van IJendoorn et al., 2022) and vertical dimension  
57 (van IJendoorn et al., 2022). These horizontal and vertical grain size variations are expected to have a

58 complex, combined effect on aeolian sediment transport, especially since grain size and sediment  
59 transport continuously interact. However, it is unknown how the spatial grain size variability influences  
60 the rate of aeolian transport towards the dunes.

61 Despite the variable transport rates for the different grain size fractions available in beach sediment,  
62 aeolian models (e.g., Hoonhout and de Vries, 2016; van Dijk et al., 1999; Roelvink and Costas, 2019,  
63 Hallin, et al., 2019c) are typically simplified by using a single fraction throughout the model domain (e.g.,  
64 Hallin, et al., 2019b; Hoonhout & de Vries, 2016; van der Wal, 2000b). However, some models can  
65 simulate multi-fraction transport, including the effect of sorting and the associated changes to the grain  
66 size distribution in the bed. An example of such a model is Aeolis, a process-based aeolian sediment  
67 transport model. The model has been used for multi-fraction simulations (e.g. Hoonhout & de Vries,  
68 2016, 2019) but the difference in transport rates compared to single-fraction simulations has not yet  
69 been fully quantified.

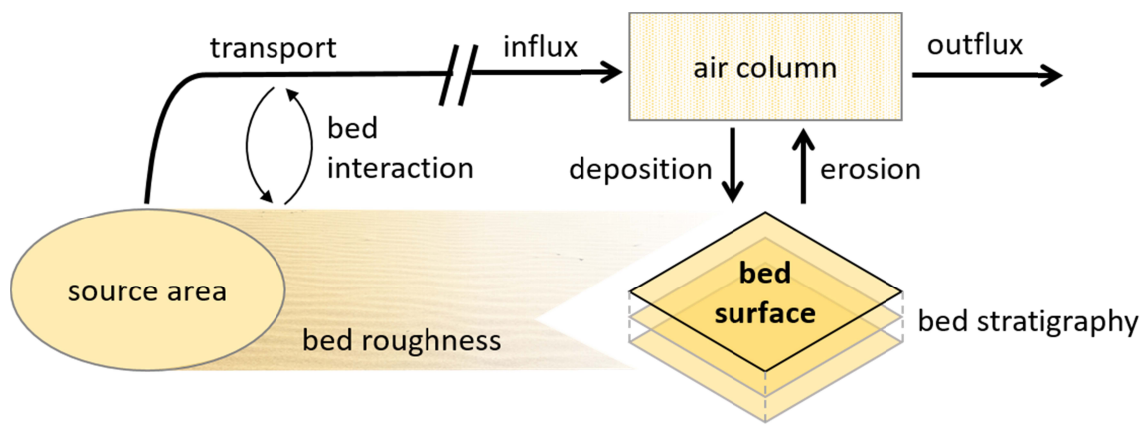
70 We hypothesize that the inclusion of multi-fraction transport and spatial grain size variations in aeolian  
71 transport simulations has a considerable effect on the calculated sediment transport. Investigating these  
72 effects in an aeolian sediment transport model can provide new insights into the functioning of the  
73 aeolian sediment transport chain. Additionally, quantifying the effects of grain size is expected to  
74 provide important recommendations for grain size as an input parameter in future aeolian transport  
75 modeling that is used for coastal dune development predictions. This quantification can also impact the  
76 use of grain size as a design parameter in the implementation of interventions in the coastal dune  
77 system (e.g., Kroon et al., 2022).

78 This research investigates to what extent sorting in multi-fraction sediment transport modeling and  
79 spatial grain size variations impact aeolian sediment transport. The important processes in the aeolian  
80 sediment transport chain are discussed in Section 2.1. The choice for a numerical model as study tool is  
81 explained in Section 2.2. The numerical implementation of different grain size scenarios that were  
82 simulated are presented in Section 3. In Section 4, the aeolian transport rates that resulted from the  
83 different grain size scenarios are presented. These results are discussed in Section 5 and the conclusions  
84 are drawn in Section 6.

## 85 **2. Background**

### 86 **2.1. Modeling the aeolian sediment transport chain**

87 Model concepts of the impact of multi-fraction transport and spatial grain size variations require that all  
 88 relevant aeolian sediment transport processes are represented in the model (Figure 1). The bed  
 89 stratigraphy consists of vertical layering with varying grain size distributions (van IJendoorn et al. 2022).  
 90 The wind forcing, the horizontal influx (upwind) and outflux (downwind) of sediment, and the sediment  
 91 available at the bed surface determine the rate of deposition/erosion that occurs (de Vries, et al., 2014a;  
 92 Houser, 2009). High wind scenarios increase the probability of erosion, however, coarse sediment at the  
 93 surface can impede pickup of sediment when armoring occurs (Gao et al., 2016; McKenna Neuman &  
 94 Bédard, 2017).



95  
 96 Figure 1 – Conceptual representation of the interaction between grain size on the bed surface and in the air  
 97 column during aeolian sediment transport on the beach.

98 Additionally, bed roughness and the fetch effect may impact whether erosion or deposition takes place.  
 99 A larger bed roughness increases the transport capacity (Bagnold, 1937b). Bed roughness can vary  
 100 greatly on the beach as the bed characteristics are variable and dynamic (Bristow et al., 2022; Field &  
 101 Pelletier, 2018; Owen, 1964; Sherman, 1992; van Rijn & Strypsteen, 2020). The fetch effect describes  
 102 how the sediment concentration in the air column increases downwind from the start of the domain  
 103 until fully developed transport is reached (Bauer & Davidson-Arnott, 2002; Delgado-Fernandez, 2010;  
 104 Gillette et al., 1996). Fully developed transport occurs when there is no additional pickup of sediment  
 105 anymore and the influx and outflux at a certain location are equal. Erosion and deposition of sediment  
 106 results from the difference between actual and equilibrium transport.

107 In case of erosion, the change in bed surface grain size will be dominated by the bed stratigraphy,  
 108 especially as underlying sediment layers can be exposed and armor layers can form (Hoonhout and de  
 109 Vries, 2016). In the case of deposition, the change in bed surface grain size will be dominated by the  
 110 grain size of the sediment in the air column. The sediment composition in the air column is determined

111 by processes that occur upwind of the bed surface location. The sediment in the air column was picked  
112 up from the source area during antecedent wind conditions and was transported towards the bed  
113 surface location (i.e. advection). During this transport, bed interaction (i.e. the splash process) might  
114 have resulted in an exchange of sediment between the air and the bed (Anderson & Haff, 1988). This  
115 exchange can alter the grain size distribution of the sediment in the air column depending on the  
116 sediment composition of the beach between the source area and the bed surface location (Dong et al.,  
117 2004).

## 118 **2.2. Studying the role of grain size in the sediment transport chain**

119 In the field, it is difficult to distinguish the effect of grain size variability from other varying  
120 environmental conditions, such as the wind field, bedforms, and surface moisture. Field measurements  
121 are often limited to a single location, which means they can show temporal patterns in grain size  
122 composition that are related to transport processes occurring upwind (Cohn et al., 2022; Field &  
123 Pelletier, 2018). Furthermore, it is difficult to observe the vertical bed composition at a relevant scale  
124 with non-invasive observation techniques (van IJendoorn et al., 2022). Here, modeling has a major  
125 advantage as it allows the recording and investigation of the transport chain, including the source area,  
126 advective transport through the air, and bed surface grain size throughout the domain.

127 The numerical aeolian sediment transport model AeoliS was selected as a tool to simulate the effect of  
128 grain size on aeolian transport in this research. AeoliS provides a systematic approach to studying  
129 spatiotemporal grain size variations. Distinguishing the impact of grain size from the many other factors  
130 that affect aeolian sediment transport on the beach is challenging. Therefore, wind tunnel experiments,  
131 in which the environmental conditions can be controlled, have been used to isolate individual aspects of  
132 aeolian sediment transport (e.g., grain size by Bagnold, 1937a, and shells by McKenna Neuman et al.,  
133 2012). However, it would be difficult if not impossible to set up experiments with complex bed  
134 composition variations at reasonable monetary, time, and labor costs. Numerical modeling provides an  
135 opportunity to gain useful insights into this type of variations at relatively low cost.

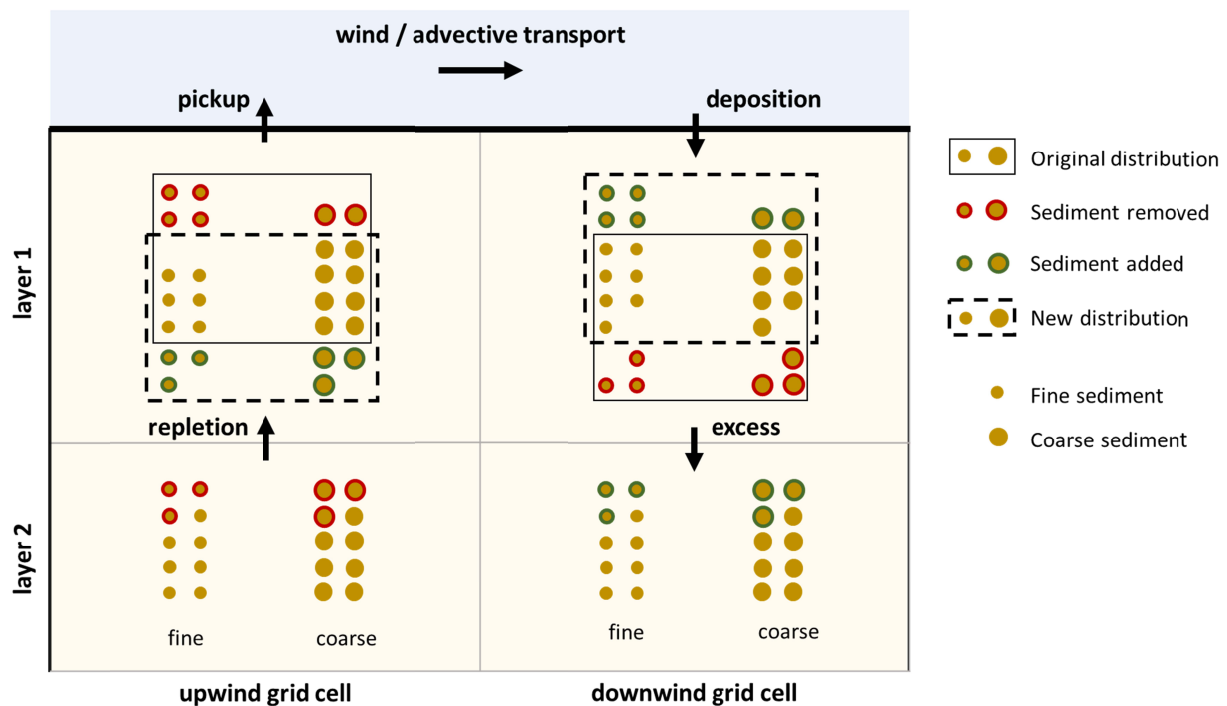
## 136 **3. Methods**

### 137 **3.1. Model description**

138 The multi-fraction approach of the AeoliS model makes it suitable to study the effect of grain size  
139 variations on aeolian transport. The sediment bed in the model consists of a user-defined number of  
140 vertical layers and horizontal grid cells. The definition of vertical layers is crucial for describing the

141 process of coarsening and fining and its associated vertical grain size gradients in the model. The bed  
 142 composition, which is the initial spatial grain size variation of the bed throughout the domain, can be  
 143 prescribed in the latest version of the model (AeoLiS v2.1.0 by AeoliS Development Team, 2022).  
 144 Transport, erosion and deposition are calculated for each grain size fraction individually (Figure 2),  
 145 allowing for surface armoring to occur as finer grains are removed, and coarse grains stay behind  
 146 (Hoonhout & de Vries, 2016).

147



148

149 Figure 2 – Schematization of the implementation of discrete layering in AeoliS and the effects of erosion and  
 150 deposition on the grain size distribution. The total mass in each grid cell of each layer is normalized. This  
 151 normalization is represented by the fact that the grain size distribution in each grid cell (indicated by solid and  
 152 dashed, black rectangles) should contain exactly 20 sediment grains. In the upwind grid cell, the bed surface layer  
 153 shows coarsening due to differential erosion of the sediment fractions. In the downwind grid cell, the bed surface  
 154 layer shows fining because the deposited sediment is a reflection of the predominantly fine sediment available in  
 155 the air column. The movement of repletion sediment in the upwind grid cell is dependent on the grain size  
 156 distribution in layer 2, whereas the movement of excess sediment in the downwind grain cell is dependent on the  
 157 original distribution in layer 1. Adapted from Hoonhout & Vries (2016).

158 In AeoliS, the equilibrium transport rate for each grain size fraction is calculated based on an adapted  
 159 version of the Bagnold equation (Bagnold, 1937b), formulated as

160

$$Q = C \frac{\rho_a}{g} (u_* - u_{t,*})^3 \quad (1)$$

161 in which  $Q$  (kg/m/s) is the aeolian sediment transport rate in the case of saturated transport, where  $C$  (-)  
162 is a constant equal to 1.5 that accounts for sediment gradation,  $\rho_a$  (kg/m<sup>3</sup>) is the density of air, and  $g$   
163 (m/s<sup>2</sup>) is the gravitational constant. The  $u_*$  is the surface shear velocity which represents the force  
164 exerted on the surface by the wind. The  $u_{t,*}$  is the threshold shear velocity which represents the shear  
165 velocity at which grains at the surface start to move (initiation of motion).

166 The threshold shear velocity is expressed as

167

$$u_{t,*} = A \sqrt{\frac{\rho_s - \rho_a}{\rho_a} g d} \quad (2)$$

168 in which  $\rho_s$  (kg/m<sup>3</sup>) is the density of the sediment,  $d$  is the grain size diameter, and  $A$  is a constant  
169 coefficient equal to 0.085. The shear velocity is expressed as

170

$$u_* = u_w \frac{\kappa}{\ln \frac{z}{z_0}} \quad (3)$$

171 in which  $u_w$  (m/s) is the wind velocity at height  $z$  (m) and  $z_0$  (m) is the aerodynamic roughness. The  $\kappa$  (-)  
172 represents the Von Karman constant. The  $z_0$  depends on the surface characteristics of the bed (i.e., the  
173 bed roughness). It should be noted that, in this research, the Nikuradse roughness method was used to  
174 calculate the aerodynamic roughness ( $z_0 = \frac{d}{30}$ ), as it allows for spatially varying grain sizes to impact the  
175 bed roughness through the median grain size,  $D_{50}$ , of the bed surface in each individual grid cell.

176 The equilibrium transport rate resulting from Equation 1 is used in a 1-D advection scheme (de Vries, et  
177 al., 2014b),

$$\frac{\partial c}{\partial t} + u_z \frac{\partial c}{\partial x} = \frac{c_{sat} - c}{T}$$

178 This equation is applied to calculate the sediment mass per unit area  $c$  (kg/m<sup>2</sup>) throughout time,  
179 indicated as  $t$  (s), and space, indicated as  $x$  (m). The  $u_z$  (m/s) represents the wind velocity at height  $z$  (m).  
180 The bed exchange, which consists of erosion and deposition, is determined as the difference between  
181 the saturated sediment concentration  $c_{sat}$  (kg/m<sup>2</sup>) and the instantaneous sediment concentration  $c$  (i.e.,  
182 the sediment concentration already present in the air) divided by an adaptation time scale  $T$  (usually 1  
183 s). The adaptation time scale results in a simulation of the fetch effect (e.g., Bauer & Davidson-Arnott,  
184 2003; Gillette et al., 1996), where the sediment concentration increases downwind from the start of the

185 domain. The increase to the maximum sediment concentration (i.e., where the normalized sediment  
186 concentration equals 1) requires a longer fetch with larger wind speeds and finer grain sizes as the  
187 saturated sediment concentration increases. Additionally, the bed exchange is maximized by the  
188 sediment that is available at the bed.

189 For this study, the AeoliS model was extended with the capability to input spatially varying bed grain  
190 size properties both in the horizontal (cross-shore and longshore) and vertical domains. The source code  
191 and documentation are open-source (<https://github.com/openearth/aeolis-python>). More details on  
192 the model concepts in AeoliS and their numerical implementation can be found in De Vries, et al.  
193 (2014b) and Hoonhout & Vries (2016).

194 The set-up of the model used in this study was based on an idealized beach environment. The 1D  
195 domain was 200 m long with a grid size of 1 m. The seaward boundary ( $x=0$  m) had zero influx of aeolian  
196 sediment, and the landward boundary was open ( $x=200$  m), so sediment can leave the domain. In the  
197 idealized beach environment, the effect of waves and tides was excluded, and only the wind that blows  
198 over a flatbed was taken into account. The wind direction was constant, and blowing in the direction of  
199 the grid from 0 to 200 m. In all simulations, nearly all default parameters of AeoliS (v2.1.0) were used  
200 (AeoliS Development Team, 2023). Only the parameters related to different grain size scenarios and  
201 time scales (discussed in Section 3.2 and 3.3), and the bed interaction (set to 0.05, following Hoonhout &  
202 Vries (2016)) deviated from the default settings.

203 The idealized beach environment was used to create scenarios with different temporal scales and  
204 different spatial grain size variations. To enable the execution of the different scenarios two main input  
205 parameters were varied: the wind forcing and the bed composition. The impact of these variations were  
206 studied by recording the sediment flux that leaves the domain. The model setup used for all scenarios,  
207 and the python code used for the analysis and generation of the figures in this paper are freely available  
208 (van IJendoorn, 2023).

### 209 **3.2. Grain size scenarios**

210 Several grain size scenarios were tested to investigate the effect of grain size variability: single-fraction,  
211 multi-fraction, horizontal variation, and vertical layering. The different grain size scenarios were  
212 simulated over different timescales with both static and variable winds to investigate the impact of  
213 sorting and wind climate. For all scenarios, a corresponding single-fraction reference grain size was used

214 to quantify the effect of the scenario on the sediment transport. An overview of the scenarios and the  
 215 25 different cases that were formulated is presented in Table 1.

216 Table 1 – Overview of the different grain size scenarios and their associated cases, including the time scales at  
 217 which the cases were executed. The underlined time scales are not shown in the Results section because they  
 218 exhibit behavior comparable to the other time scales.

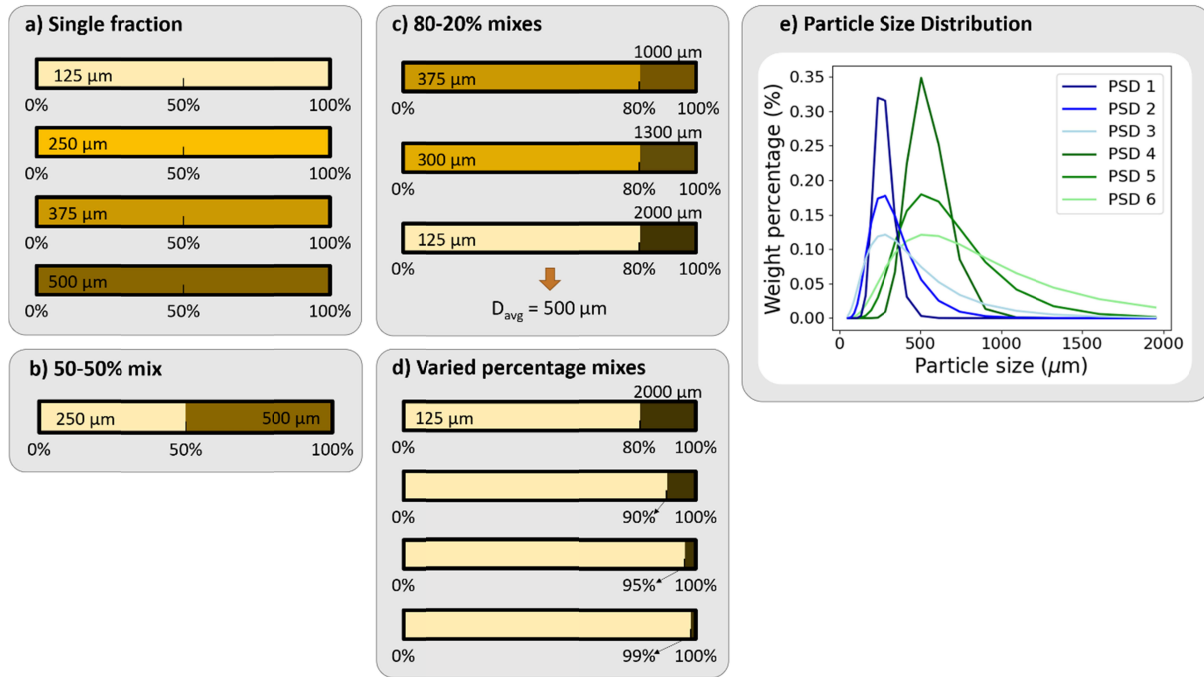
Scenario	# of cases	Case description	Time scale
Single-fraction	6	125, 250, 300, 375, 500, 1000 and 2000 $\mu\text{m}$	10 min, 1 day, 1 year
Multi-fraction	1	Two fractions	50%-50%
	3		20%-80%
	4		varied percentage
	6	Full particle size distribution	1 day, 1 year
Spatial variations	3	Horizontal	10 min, <u>1 day</u> , 1 year
	2	Vertical	10 min, 1 day, <u>1 year</u>

219

220 A single fraction scenario and a multi-fraction scenario, which included cases with two-fraction mixes  
 221 and full particle size distributions (PSDs), were executed to investigate the effect of including multi-  
 222 fraction transport in aeolian sediment transport simulations (Figure 3). For the single-fraction scenario,  
 223 cases were created with one grain size class between 125 and 2000  $\mu\text{m}$  that was the same in the entire  
 224 bed (Figure 3a). In the two-fraction mix cases, grain size classes between 125 and 2000  $\mu\text{m}$  were used.  
 225 Two grain size classes were chosen with different weights assigned to both classes for each case (Figure  
 226 3b, c and d). The percentages used in the context of grain size distributions indicate weight percentages.  
 227 The single-fraction reference for the 50-50% and 80-20% mixes was defined as the average grain size.  
 228 The single-fraction 125  $\mu\text{m}$  case was used as a reference for the varied percentage mix.

229 For the particle size distribution cases, 6 PSDs were created with Qgrain (Liu et al., 2021). The shape  
 230 parameters (i.e., mean, standard deviation, weight and skewness) of the average grain size distribution  
 231 of all samples collected in Noordwijk as presented in van IJendoorn et al. (2022) were determined by  
 232 fitting a skewed normal distribution. Subsequently, the median grain size (250 and 500  $\mu\text{m}$ ) and  
 233 standard deviation ( $\sigma = 0.32, 0.62$  and  $0.92$ ) were varied to create 6 PSDs (Figure 3e). The median grain

234 size of each PSD was used as the reference case. The full particle size distribution was expressed as the  
 235 mass weight of each grain size class with 20 classes ranging from 50 to 1950  $\mu\text{m}$ .

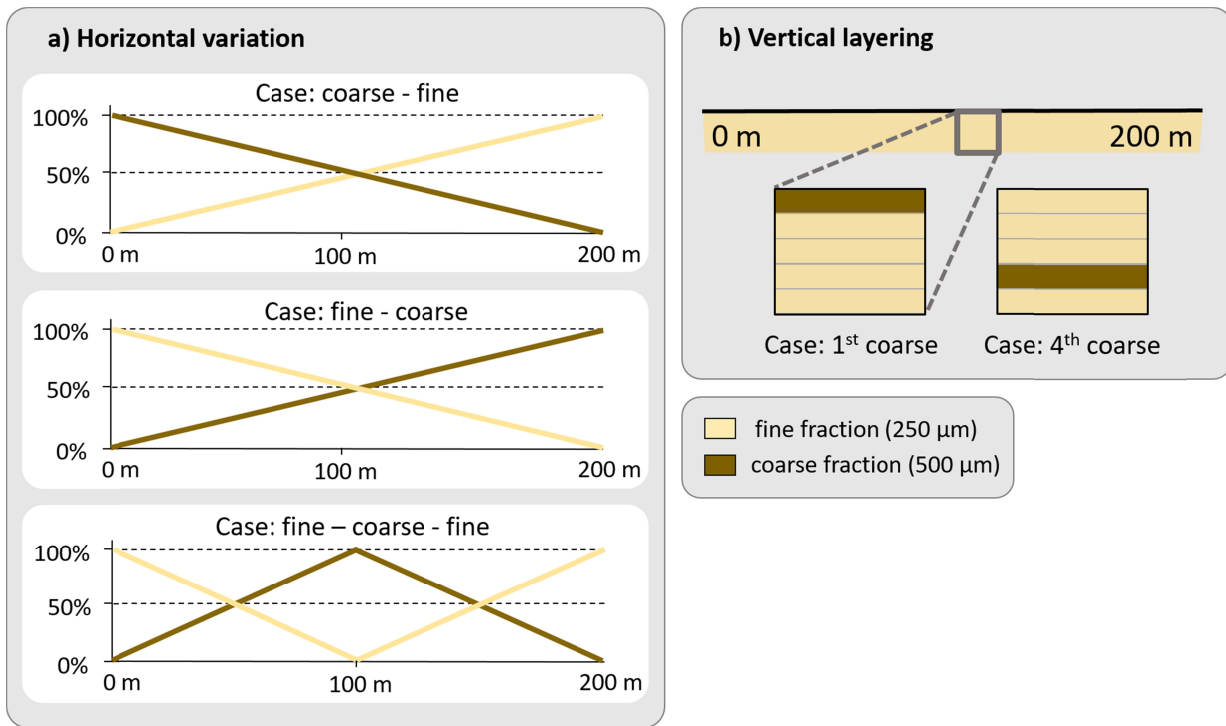


236

237 Figure 3 – Overview of the different grain size scenarios that were used in simulations with a spatially invariant  
 238 grain size. For (c) the 80-20% mixes all had the same average grain size ( $D_{\text{avg}} = 500 \mu\text{m}$ ). In (d) the varied  
 239 percentage mixes, two fixed grain size classes were used (i.e. 125 and 2000  $\mu\text{m}$ ), but the median grain size varied  
 240 as the mass distribution over two fixed grain size classes was varied. The (e) particle size distribution scenario  
 241 consisted of 6 different PSDs with a median grain size of approximately 250 (blue) or 500  $\mu\text{m}$  (green) and varying  
 242 distribution widths.

243 The effect of spatial grain size variations on aeolian sediment transport simulations was investigated  
 244 with horizontal variation and vertical layering scenarios (Figure 4). Horizontal variations were  
 245 implemented with a coarse-fine, fine-coarse and fine-coarse-fine gradient (Figure 4a). To create these  
 246 gradients, the weight of a fine fraction (250  $\mu\text{m}$ ) and a coarse fraction (500  $\mu\text{m}$ ) were varied between 0  
 247 and 100% along the domain. In all cases, the average distribution of the two fractions was 50-50%, thus,  
 248 the average grain size of 375  $\mu\text{m}$  was used as a reference case. The different spatial distributions  
 249 represent fining and coarsening gradients found in the field. Specifically, the gradient with coarse  
 250 material in the middle represents field situations where the coarsest sediments have been found on the  
 251 berm. The horizontal spatial gradients were applied to all vertical layers in the domain, including the

252 lowest one. This results in the initial grain size gradient being continuously supplied from below. This  
 253 assumes that the initial bed stratigraphy is uniform with depth.



254  
 255 Figure 4 – Overview of the different grain size scenarios that were used in simulations with a spatially varying grain  
 256 size gradients. (a) The horizontal variation scenario consisted of three different gradients where a fine (250 μm)  
 257 and coarse (500 μm) grain size class were spatially mixed. (b) In the vertical layering scenario, all layers consisted of  
 258 the fine grain size class (250 μm) apart from one coarse layer (500 μm).

259 The effect of grain size variations in the vertical dimension was investigated with a vertical layering  
 260 scenario. In this scenario, the grain size layering at the beach surface was represented by 5 layers,  
 261 consisting of either fine (250 μm) or coarse (500 μm) sediment (Figure 4b). In the first case, the upper  
 262 layer consisted of coarse sediment, whereas in the second case, the fourth layer consisted of coarse  
 263 sediment. Both cases have an average grain size of 300 μm, so a single-fraction case was executed for  
 264 comparison with the vertical layering scenario. In both cases, the fifth layer consisted of the same grain  
 265 size class (250 μm). This lowest layer determines the supply from below. Thus, by assigning the same  
 266 grain size, large deviations between the cases were prevented that would have occurred if all  
 267 superimposed sediment was eroded.

268 **3.3. Simulation time and wind forcing**

269 Runs of 10 minutes, 1 day, and 1 year were executed to assess the effect of grain size variations across  
 270 time scales. The 10-minute runs involved constant wind speeds between 0 and 30 m/s. The 1 day and 1  
 271 year academic cases were simulated with varying winds that were created with the wind generator in  
 272 AeoliS. The wind generator creates a random wind velocity time series with a given mean and maximum  
 273 wind speed using a Markov Chain Monte Carlo approach based on a Weibull distribution. A mean wind  
 274 speed of 10 m/s with a maximum wind speed of 30 m/s was used as input for the wind generator.  
 275 Generated wind speeds fluctuate on the scale of the model timestep,  $dt$ , which was varied based on the  
 276 simulation time (Table 2).

277 Table 2 – AeoliS model settings and wind input for scenarios with different temporal scales

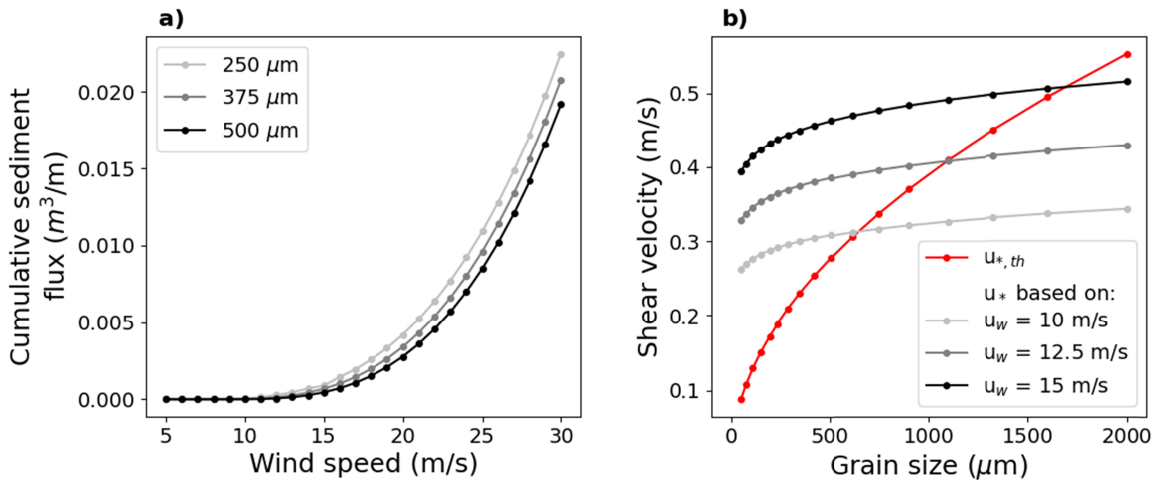
Simulation time	$dt$	Output_times	Wind regime	# of layers	Layer_thickness
10 minutes	1	10	Constant, range from 0 to 30 m/s	5	0.00005
1 day	60	600	Variable, mean 10 m/s, max 30 m/s	5	0.0001 281 282
1 year	3600	86400	Variable, mean 10 m/s, max 30 m/s	5	0.01

284 The layer thickness used in the simulations (Table 2) was scaled to the time step. This was done to avoid  
 285 sediment depletion in the surface layer during time steps with peak transport, which would influence  
 286 calculated transport rates. Increasing the resolution for the longer time scales is possible with a reduced  
 287 time step. However, this would greatly increase the computation time needed for each simulation. We  
 288 tested whether increasing the vertical resolution from 5 to 50 layers would have an effect on the 10-  
 289 minute time scale of the vertical layering scenario with a constant 10 m/s wind. The test showed that  
 290 the sediment flux remained similar (i.e., a difference < 3%). However, there were some minor  
 291 differences in the temporal trends of the pickup of the coarse and fine sediment, which were related to  
 292 (numerical) diffusion of the vertical grain size gradient in the 5 layer test. These effects might be  
 293 exacerbated at longer time scales and with the inclusion of varying wind speeds in a simulation.  
 294 Therefore, the quantitative aeolian sediment transport results that were obtained at different time  
 295 scales for each case, were not directly compared in this paper.

296 **4. Results**

297 **4.1. The transport of single-fraction sediment**

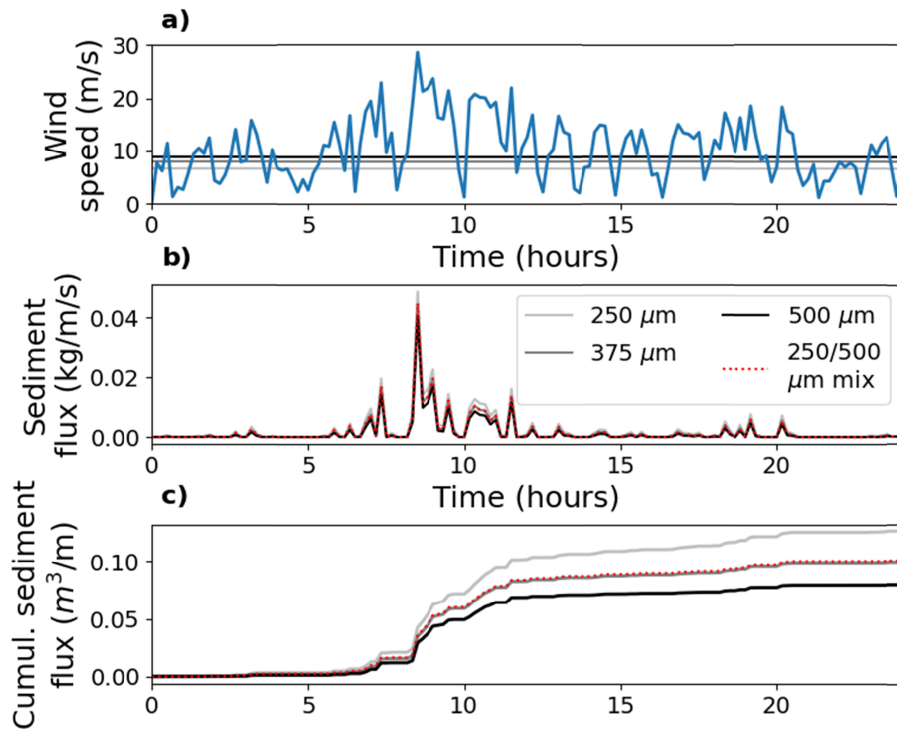
298 Distinct variations in the way different grain sizes reacted to varying wind speeds on the 10 minute time  
 299 scale were observed in the model results (Figure 5a). Below 10 m/s, the threshold for transport was  
 300 barely exceeded, and little to no sediment flux occurred for grain sizes between 250 and 500  $\mu\text{m}$ .  
 301 Between 10 and 15 m/s, the differentiation between the grain size cases was the largest. For these wind  
 302 speeds, the behavior of the shear velocity and threshold shear velocity following Equation 2 and 3 is  
 303 shown in Figure 5b. As finer grain sizes have a lower threshold velocity (red line in Figure 5a), transport  
 304 was initiated at lower wind speeds. For wind speeds above 15 m/s, sediment transport occurred in all  
 305 grain size cases. Because the shear velocity increased with the wind velocity (Equation 2) and the  
 306 sediment flux is cubically related to the difference between the shear velocity and the threshold shear  
 307 velocity (Equation 1), the transport that occurred at a 30 m/s wind speed was more than an order of  
 308 magnitude higher than that at a 15 m/s wind speed.



309  
 310 Figure 5 – (a) The cumulative sediment flux after 10 minutes for wind speeds of 0 to 30 m/s for grain sizes of 250,  
 311 375 and 500  $\mu\text{m}$ . (b) The relation between grain size and the threshold shear velocity  $u_{*,th}$  as follows from Equation  
 312 2 in red, and the relation between grain size and the shear velocity  $u_*$  for three different wind speeds as follows  
 313 from Equation 3 (greyscale lines). The shear velocity  $u_*$  varies with grain size due to the dependence of the  
 314 aerodynamic roughness  $z_0$  on the grain size in Equation 3.

315 On the 1-day time scale, a larger transport magnitude occurred for the 250 and 375  $\mu\text{m}$  cases than the  
 316 500  $\mu\text{m}$  case (Figure 6b). The difference in transport between the three cases was largest in the  
 317 moments with high wind speeds. Throughout time, the difference in the cumulative sediment flux  
 318 between the grain size cases increased (Figure 6c), which is the result of both the difference in threshold

319 velocity and the transport magnitude. For finer grain sizes, the lower threshold velocity resulted in a  
320 longer time period in which transport could occur, and in that time period, the transport was higher  
321 than that for the coarser grain sizes (Figure 6a).



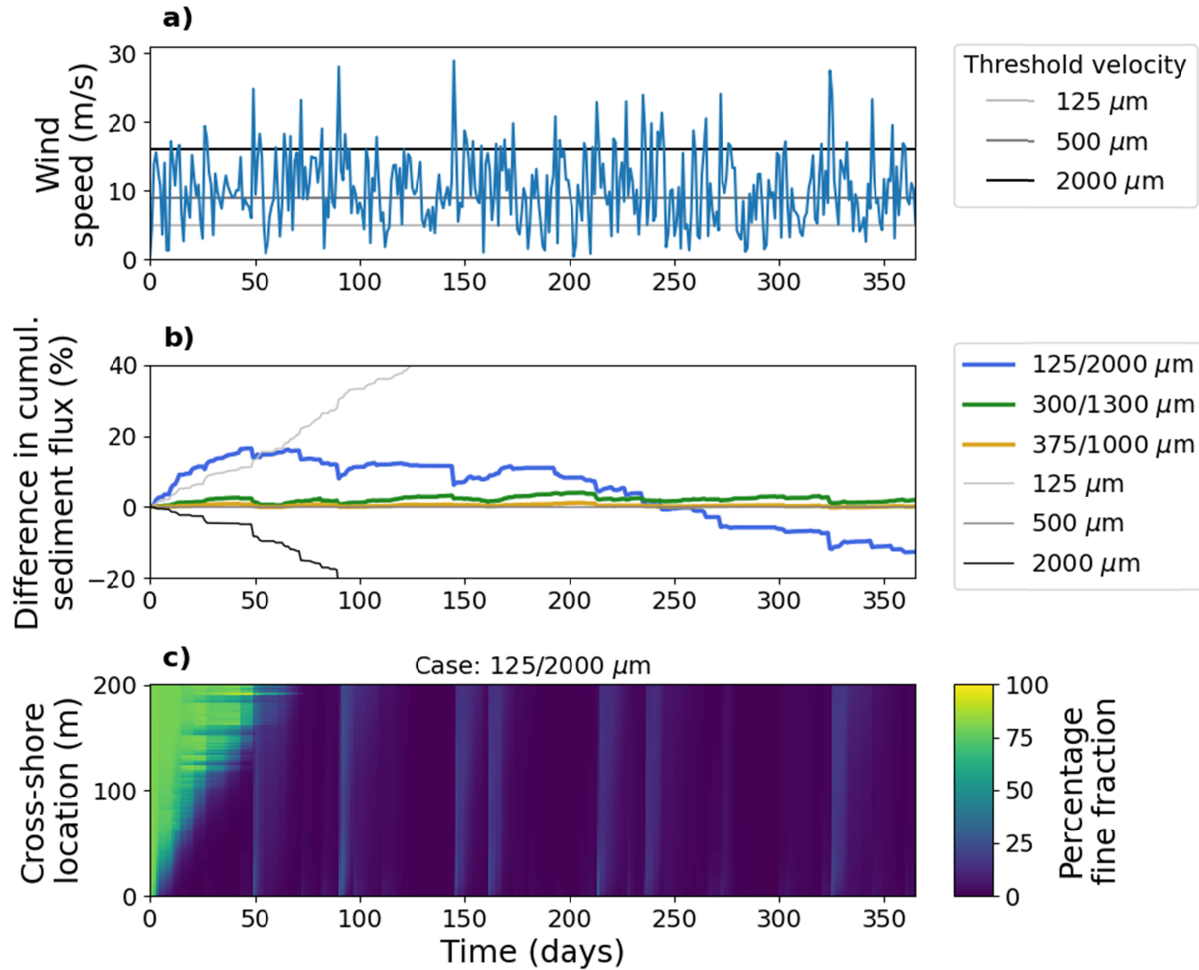
322  
323 Figure 6 – (a) One-day variable wind scenario which results in the (b) sediment flux and (c) cumulative sediment  
324 flux of the single-fraction cases of 250, 375, and 500  $\mu\text{m}$  and of a two-fraction 250/500  $\mu\text{m}$  mix (50-50% mix, Figure  
325 3b). The horizontal lines in the wind plot indicate the threshold velocity for the single-fraction case with the  
326 corresponding color in (b) and (c).

#### 327 4.2. Comparison between single-fraction and two-fraction mixes

328 The 50-50% mix with the 250 and 500  $\mu\text{m}$  sediment fractions resulted in similar transport rates as the  
329 single-fraction simulation with the average grain size of 375  $\mu\text{m}$  (Figure 6c). For the simulated wind  
330 climate, there was little effect of the coarsening of the top layer. There was some differentiation  
331 between the mix and the 375  $\mu\text{m}$  case in periods where the wind speed was around the threshold  
332 velocity of the different fractions. However, the highest wind speeds resulted in the largest contribution  
333 to the sediment flux. Thus, the differentiation at lower wind speeds was negligible on the scale of the  
334 total cumulative sediment flux during the one-day simulation. For the higher wind speeds, the larger and

335 smaller transport that occurred for the 250  $\mu\text{m}$  and 500  $\mu\text{m}$  fractions in the mix balanced each other,  
336 making the resulting cumulative transport comparable to the 375  $\mu\text{m}$  case. This equalization may occur  
337 because the shear velocity and threshold shear velocity in Figure 5b show approximately linear trends  
338 for this relatively limited grain size range. At the yearly time scale, the behavior of the two-fraction mix  
339 was also closely replicated with a single fraction equal to the average grain size of the mix.

340 The effect of armoring was further investigated with 80-20% mixes of varying grain sizes (125/2000  $\mu\text{m}$ ,  
341 300/1300  $\mu\text{m}$ , and 375/1000  $\mu\text{m}$ ) with a constant average grain size equal to 500  $\mu\text{m}$ . At a yearly  
342 timescale, the cumulative sediment flux varied for the different mixes (Figure 7). The 375/1000  $\mu\text{m}$  case  
343 aligned with the result of the average grain size, the 300/1300  $\mu\text{m}$  mix was slightly larger, and the  
344 125/2000  $\mu\text{m}$  mix showed larger deviations. At the start of the year, the cumulative sediment flux of the  
345 125/2000  $\mu\text{m}$  mix exceeded that of the average grain size. Within the first 50 days, it even exceeded the  
346 cumulative sediment flux of the single-fraction 125  $\mu\text{m}$  case. The explaining mechanism is the increase  
347 of the aerodynamic roughness in the mix that was caused by the coarse fraction. A larger aerodynamic  
348 roughness increases the shear velocity (greyscale lines in Figure 5b) and, thus, the transport capacity  
349 which is dependent on the difference between the shear velocity and the threshold shear velocity  
350 (Equation 1). After the 50-day period, this increased transport capacity was counteracted by the  
351 coarsening of the bed surface (Figure 7), and the cumulative sediment flux progressively got closer to  
352 the reference case. After 240 days, the cumulative transport of the 125/2000  $\mu\text{m}$  case became even  
353 lower than the reference case, eventually resulting in approximately 15% less cumulative transport at  
354 the end of the year. Similar fluctuations in the difference in cumulative sediment flux occurred for the  
355 300/1300  $\mu\text{m}$  mix, although, the cumulative sediment flux was never less than the reference case.

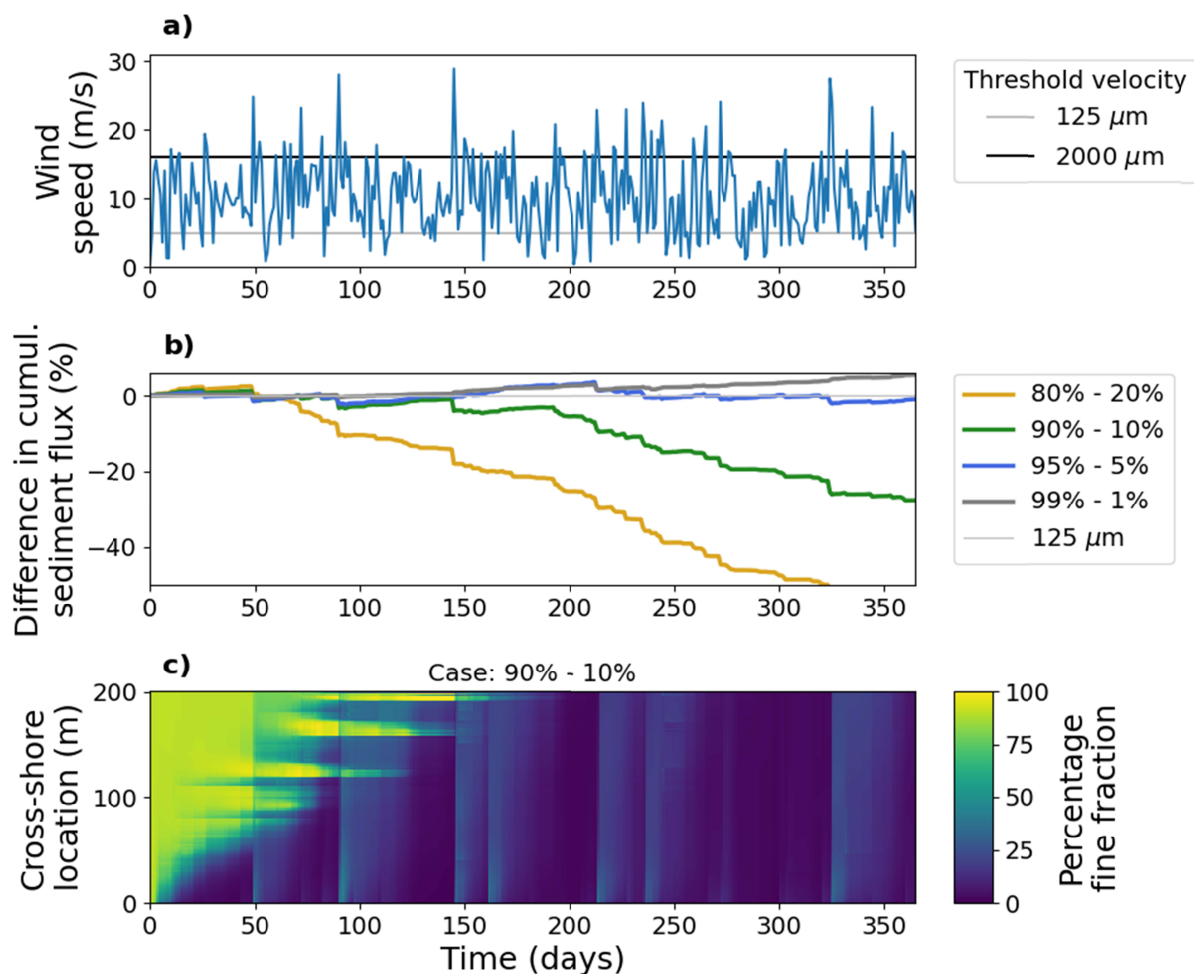


356 Figure 7 - (a) 1-year variable wind scenario. The horizontal lines in the wind plot indicate the threshold velocity for  
 357 single-fraction cases with colors corresponding to the sediment fluxes in (b). (b) Cumulative sediment flux of the  
 358 single-fraction cases of 125  $\mu\text{m}$  (light grey), 500  $\mu\text{m}$  (grey), and 2000  $\mu\text{m}$  (black), compared to the cumulative  
 359 sediment flux that occurs for the 80-20% mixes (Figure 3c) in blue, green, and yellow that all have an average grain  
 360 size of 500  $\mu\text{m}$ . Note that the single-fraction case of 500  $\mu\text{m}$  is used as the reference case. (c) Time-stack of the  
 361 development of the percentage of fine fraction that is present in the top layer of the bed surface for the 125/2000  
 362  $\mu\text{m}$  mix through time (x-axis) and space (y-axis).  
 363

364 **4.3. The effect of coarse fraction percentage on sediment transport**

365 Not only the size but also the relative percentage of the coarse fraction affects the cumulative sediment  
 366 flux (Figure 8). The effect of the percentage of coarse fraction was investigated by varying the coarse  
 367 sediment percentage between 1 and 20% in a 125/2000  $\mu\text{m}$  mix (Figure 3d). The 80-20% case showed a  
 368 strong deviation in the cumulative sediment flux compared to the reference case (100% 125  $\mu\text{m}$ )  
 369 resulting in a decrease in the yearly cumulative transport rate of more than 50% (Figure 8b). The

370 decrease in transport due to armoring occurred from 70 days and onwards. For the 90-10% case, it took  
 371 150 days for this deviation to occur, and the deviation after a year was smaller, at approximately 30%  
 372 less transport than the reference case. The cases where only 1 or 5% of coarse fraction was present did  
 373 not show a considerable deviation from the sediment flux of the fine fraction within the 1-year time  
 374 frame. All cases showed how wind speed peaks affect the cumulative sediment flux. The wind speed  
 375 peaks cause mobilization of the coarse fraction at the bed surface, which exposes finer fractions that are  
 376 more easily transported (Figure 8c).

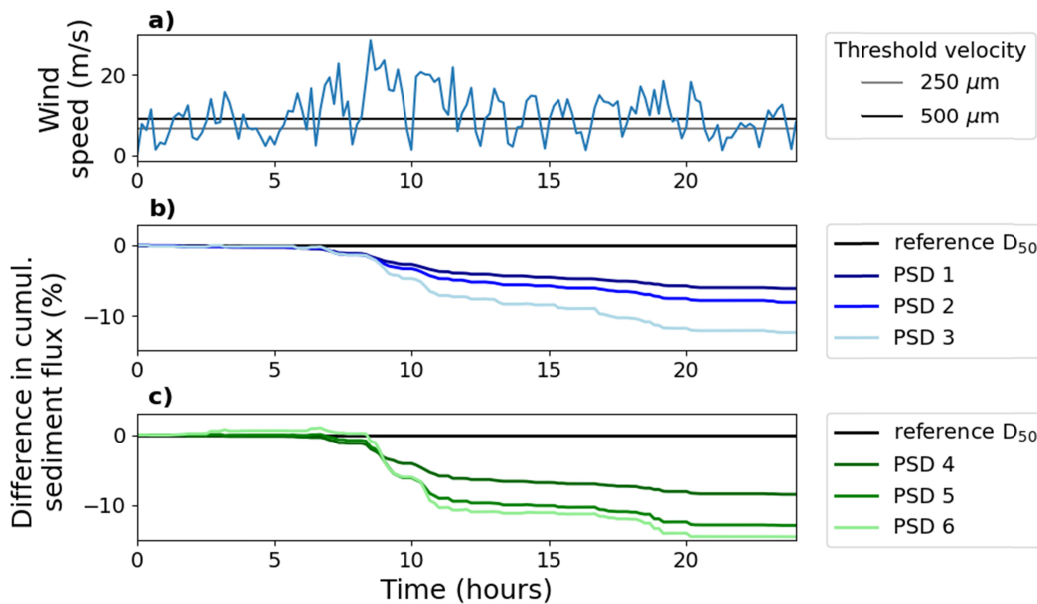


377  
 378 Figure 8 – (a) 1-year variable wind scenario. The horizontal lines in the wind plot indicate the threshold velocity for  
 379 the single-fraction case of 125 μm (light grey) and 2000 μm (black). (b) Cumulative sediment flux of the reference  
 380 single-fraction case of 125 μm (light grey), compared to the cumulative sediment flux that occurs for two-fraction  
 381 mixes in yellow, green, blue, and grey that consist of varying percentages of the 125 and 2000 μm fractions (Figure  
 382 3d). (c) Time-stack of the development of the percentage of fine fraction that is present in the top layer of the bed

383 surface through time (x-axis) and space (y-axis), visualized for the 125/2000  $\mu\text{m}$  mix that starts with 90% fine and  
384 10% coarse fraction.

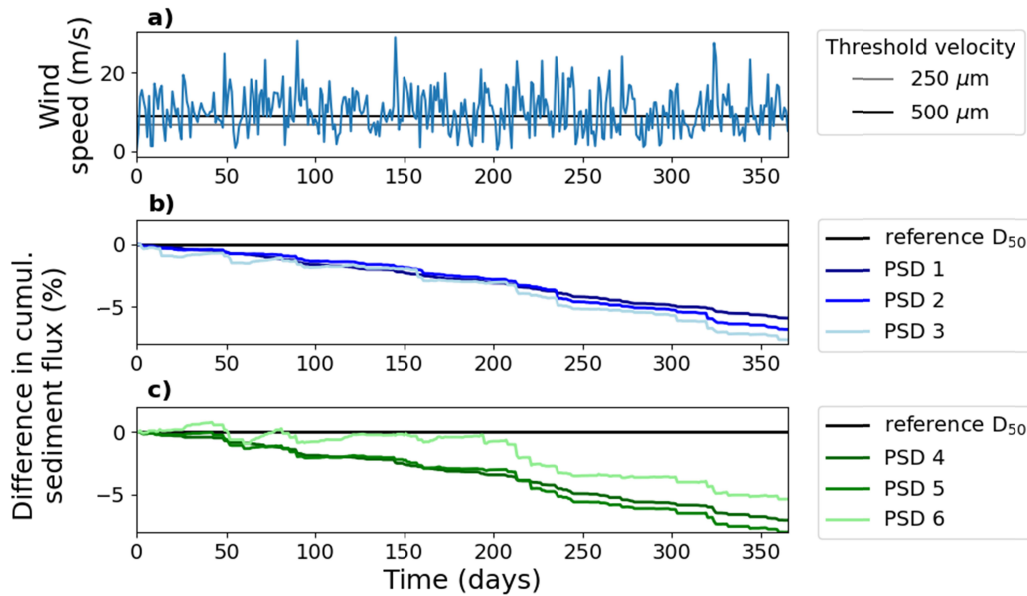
#### 385 4.4. The effect of different particle size distributions on sediment transport

386 Compared to the two fraction mixes, the simulations with full particle size distributions resulted in less  
387 deviation from the reference case (median grain size of the PSD). The maximum difference in cumulative  
388 sediment flux was 15% and 7.5% less transport after the 1-day (Figure 9) and 1-year period (Figure 10),  
389 respectively. Overall, all PSDs showed comparable trajectories, except for PSD 6, which has the widest  
390 distribution. In the 1-day period, PSD 6 showed several hours with a larger cumulative sediment flux  
391 than the reference grain size. This might have been related to a relatively large aerodynamics roughness  
392 and fine fraction abundance, caused by the shape of PSD 6 (Figure 3e). In the 1-year period, PSD 6  
393 remained relatively close to the reference grain size up until day 200, whereas the other PSDs already  
394 showed significant deviations near the start of the simulation. Again, this behavior might be caused by  
395 the balance between the presence of coarse and fine fractions in the grain size distribution.



396

397 Figure 9 – (a) 1-day variable wind scenario. The horizontal lines in the wind plot indicate the threshold velocity for  
398 the single-fraction case of 250  $\mu\text{m}$  (grey) and 500  $\mu\text{m}$  (black). (b) and (c) Cumulative sediment flux of each tested  
399 particle size distribution (PSD) as shown in Figure 3e, compared to the reference case (black). For each PSD, the  
400 reference case corresponds to the median grain size of the PSD. The blue colors in (b) have a median grain size of  
401 around 250  $\mu\text{m}$ , the green colors in (c) have a median grain size around 500  $\mu\text{m}$ .



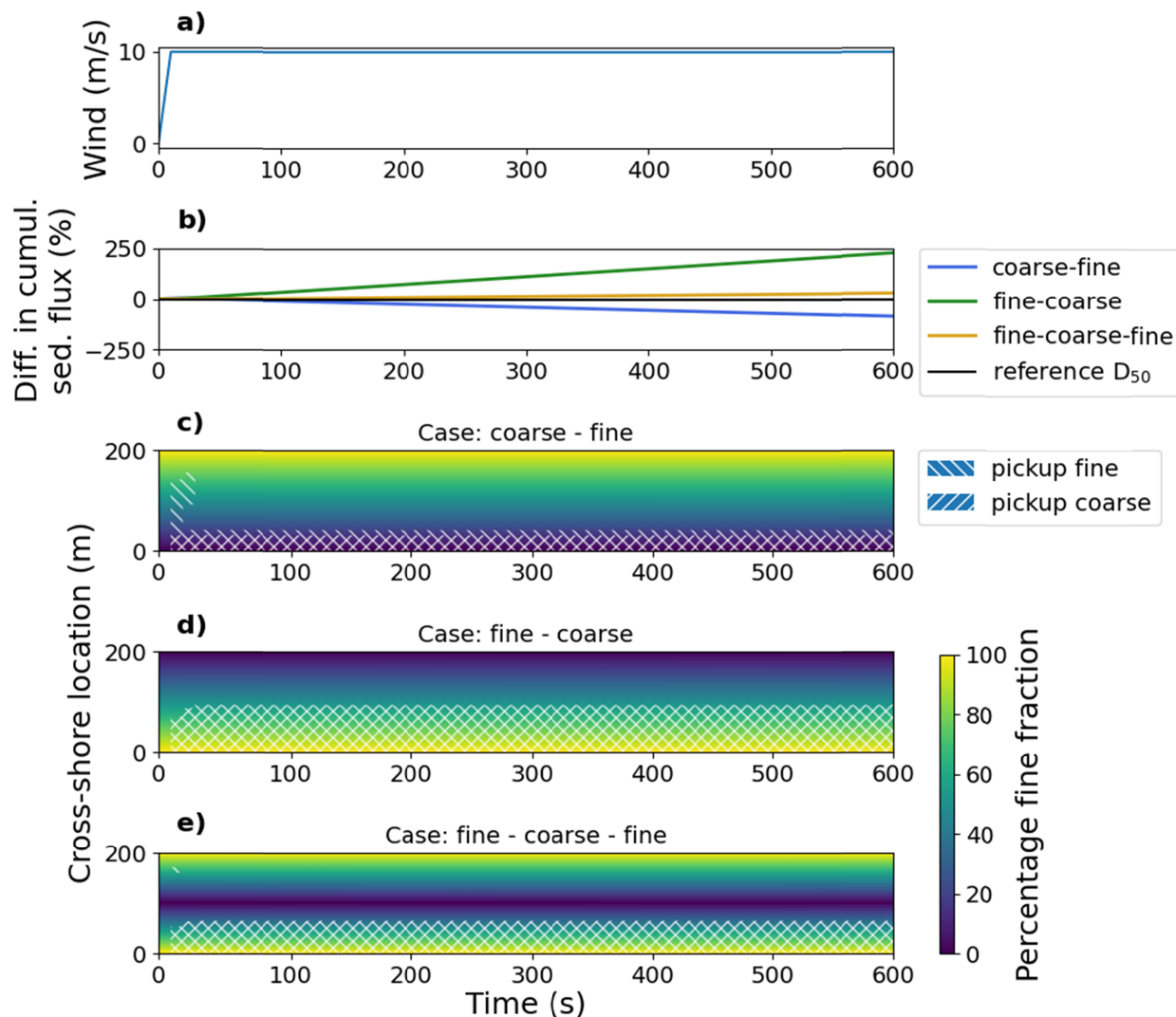
402

403 Figure 10 – (a) 1-year variable wind scenario. The horizontal lines in the wind plot indicate the threshold velocity  
 404 for the single-fraction case of 250  $\mu\text{m}$  (grey) and 500  $\mu\text{m}$  (black). (b) and (c) Cumulative sediment flux of each  
 405 tested particle size distribution (PSD) as shown in Figure 3e, compared to the reference case (black). For each PSD,  
 406 the reference case corresponds to the median grain size of the PSD. The blue colors in (b) have a median grain size  
 407 of around 250  $\mu\text{m}$ , the green colors in (c) have a median grain size around 500  $\mu\text{m}$ .

408 **4.5. The impact of grain size variability in the horizontal dimension**

409 The horizontal variation cases with different spatial gradients showed distinctly different cumulative  
 410 sediment fluxes when simulated for a 10-minute period with a constant 10 m/s speed. The finer the  
 411 sediment at the start of the domain, the higher the cumulative sediment flux (Figure 11). In Figure 11b,  
 412 c, and d, the erosion area in the domain is indicated with white hatching, where leftward leaning  
 413 hatching indicates pickup of the fine fraction and rightward leaning hatching indicates pickup of the  
 414 coarse fraction. The variation in the cross-shore expanse of the erosion area between the different  
 415 scenarios indicates a variation in the fetch length, which could have been caused by a difference in the  
 416 magnitude of the equilibrium transport. Coarse sediment resulted in a lower equilibrium transport  
 417 magnitude (Equation 1), so based on the implementation of the adaptation timescale, the distance  
 418 needed to reach the equilibrium transport was smaller than with fine sediment at the start of the  
 419 domain which is related to a larger equilibrium transport. The larger bed roughness that occurred for  
 420 the coarse sediment counteracted this effect slightly. In conclusion, the fetch length is shorter when  
 421 coarser sediment is present at the start of the domain, and as fully developed transport was reached at

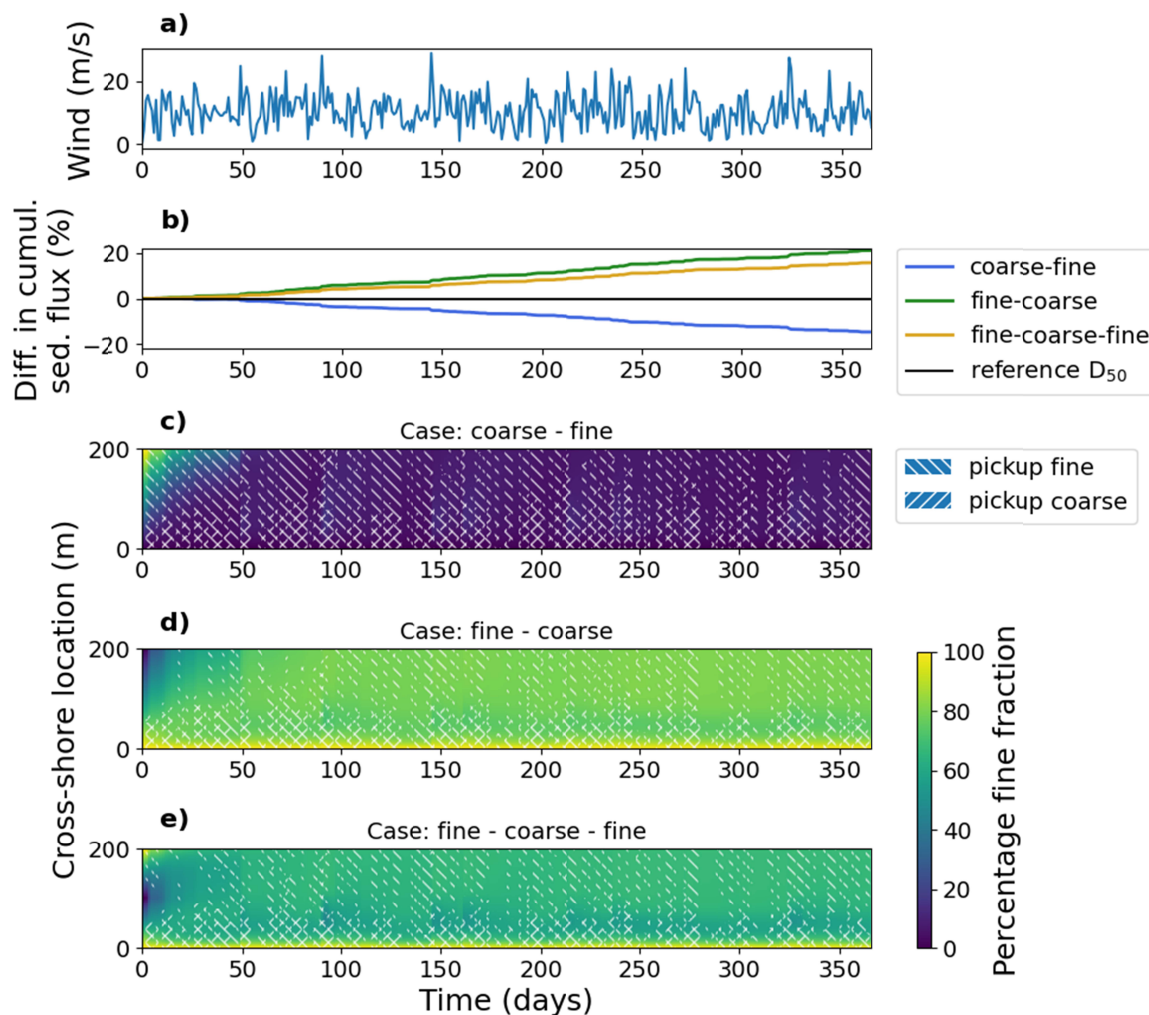
422 the end of the erosion area, there was no significant impact of the bed surface gain size composition  
 423 further along the domain.



424  
 425 Figure 11 - (a) Cumulative sediment fluxes under a 10-minute, constant 10 m/s wind speed for the horizontal  
 426 variation scenario (Figure 4a), which includes a coarse to fine (blue), fine to coarse (green) and fine to coarse to  
 427 fine (yellow) gradient, compared to the reference grain size of 375  $\mu\text{m}$  (black). Time-stack of the development of  
 428 the percentage of fine fraction that is present in the top layer of the bed surface for the (b) coarse to fine, (c) fine  
 429 to coarse and (d) fine to coarse to fine case.

430 The 1-day and 1-year simulations of the horizontal grain size variations resulted in similar sediment flux  
 431 behavior. The coarse-fine case resulted in less transport than the reference  $D_{50}$  and the fine-coarse and  
 432 fine-coarse-fine cases resulted in more transport (Figure 12). The bed surface layer development of the

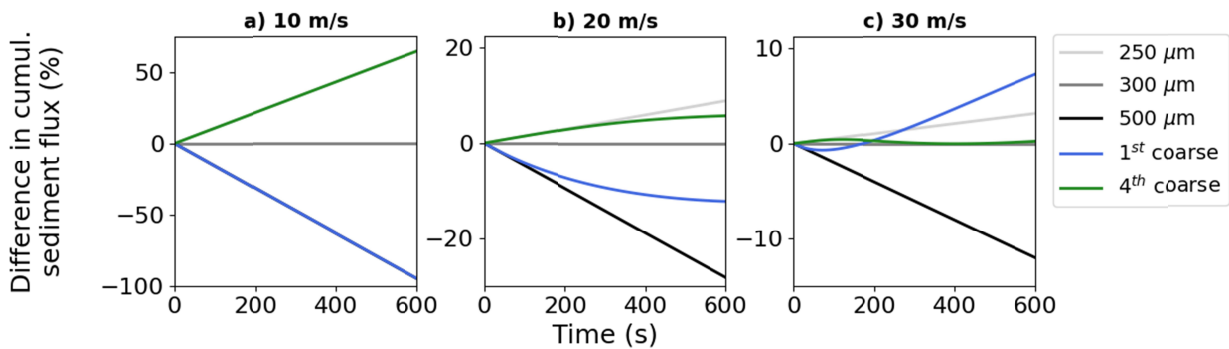
433 coarse-fine case showed coarsening of the surface (Figure 12c), whereas the fine-coarse case showed  
 434 fining (Figure 12d). For each case, a unique cross-shore equilibrium bed composition developed at the  
 435 bed surface. The occurrence of pickup throughout the domain seemed most strongly related to the wind  
 436 speed. However, after the formation of the equilibrium grain size gradient, the region with pickup  
 437 became much larger for both periods and all cases.



438  
 439 Figure 12 - (a) 1-year variable wind scenario. (b) Cumulative sediment fluxes of the horizontal variation scenario  
 440 (Figure 4a), which includes a coarse to fine (blue), fine to coarse (green) and fine to coarse to fine (yellow)  
 441 gradient, compared to the reference grain size of 375  $\mu\text{m}$  (black). Time-stack of the development of the  
 442 percentage of fine fractions that is present in the top layer of the bed surface for the (b) coarse to fine, (c) fine to  
 443 coarse and (d) fine to coarse to fine case.

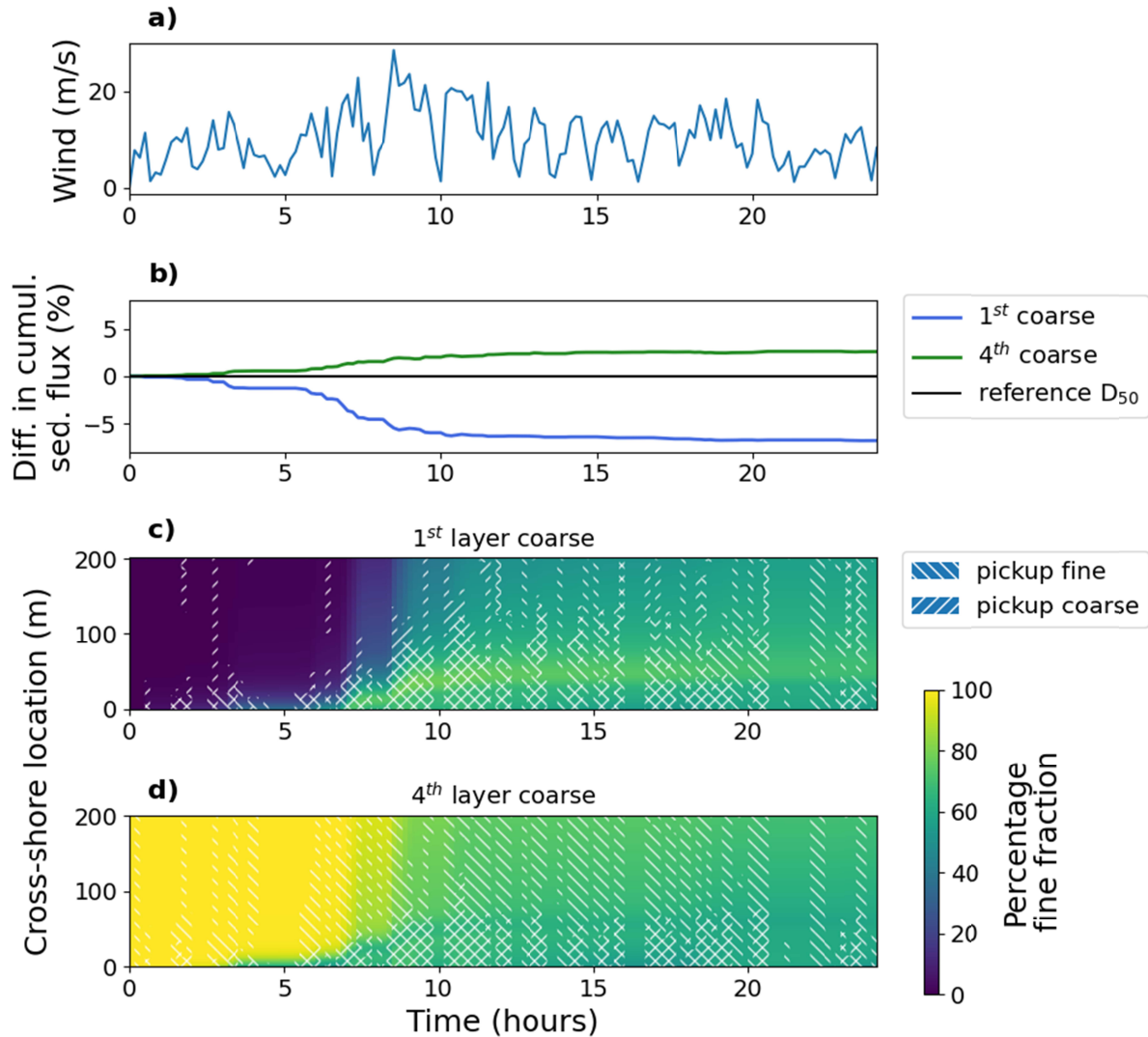
444 **4.6. Sediment transport variations due to vertical grain size variability**

445 The vertical grain size layering directly affected the amount and timing of aeolian transport during the  
 446 different time scales. For the 10-minute simulations, varying behavior was observed depending on the  
 447 wind speed and the vertical location of the coarse layer (Figure 13). At a wind speed of 10 m/s, little  
 448 transport occurred due to the relatively low wind speeds, and the grain size fraction in the upper layer  
 449 of both cases dominated the cumulative sediment flux (Figure 13a). At 20 m/s, the removal of the coarse  
 450 and fine fraction for the 1<sup>st</sup> layer coarse and 4<sup>th</sup> layer coarse case, respectively, resulted in a reduction of  
 451 the difference in the cumulative sediment flux compared to the reference grain size (Figure 13b). At 30  
 452 m/s, both the fine and coarse sediment were easily mobilized by the wind, resulting in a considerably  
 453 lower difference in cumulative sediment flux compared to the reference grain size (Figure 13c).



454 Figure 13 - Cumulative sediment fluxes of the vertical layering scenario (Figure 4b) compared to the reference  
 455 grain size 300 μm (grey) for 10-minute simulations with a constant wind speed of (a) 10 m/s, (b) 20 m/s, and (c) 30  
 456 m/s. The scenario includes the case where the top layer (blue) and the fourth layer (green) consisted of a coarse  
 457 fraction (500 μm). The other layers consisted of a fine fraction (250 μm). For comparison, the cumulative sediment  
 458 flux of the single-fraction case of 250 (light grey) and 500 μm (black) are shown.  
 459

460 On the scale of a 1-day simulation, the main differentiation in the cumulative sediment flux between the  
 461 vertical layering cases and the reference grain size (Figure 14b) occurred during the wind peak between  
 462 hours 5 and 10 (Figure 14a). This wind peak caused the coarse and fine sediment of, respectively, the 1<sup>st</sup>  
 463 coarse case and 4<sup>th</sup> coarse case to be removed from the surface layer (Figure 14 c and d). Subsequently,  
 464 a relatively stable spatial grain size gradient formed, and the difference in cumulative sediment flux  
 465 showed limited change for both cases. As the spatial grain size gradient of the bed surface layer  
 466 changed, the extent of the pickup area, especially for the coarse fraction, increased. Overall, the 1-year  
 467 simulation, showed comparable trends to the 1-day simulation, although the difference in cumulative  
 468 sediment flux compared to the reference was lower (around 1% vs. 5%).



469

470 Figure 14 - (a) 1-day variable wind scenario. (b) Cumulative sediment fluxes of the vertical layering scenario (Figure  
 471 4b) compared to the reference grain size 300  $\mu\text{m}$  (black). The scenario includes case 1 (blue), where the top layer  
 472 consisted of a coarse fraction, and case 2 (green), where the fourth layer consisted of a coarse fraction (500  $\mu\text{m}$ ).  
 473 The other layers consisted of a fine fraction (250  $\mu\text{m}$ ). Time-stack of the development of the percentage of fine  
 474 fractions that is present in the top layer of the bed surface for (b) case 1 and (c) case 2.

## 475 5. Discussion

### 476 5.1. Using a single-fraction representative grain size in aeolian sediment transport modeling

477 The cumulative sediment flux calculated with multi-fraction transport and its approximation with a  
 478 single-fraction reference grain size were similar on time scales of days to years. There only was a  
 479 considerable impact on the yearly cumulative transport when a relatively large content of coarse grains,

480 >10% of 2000  $\mu\text{m}$  sediment, was present. The full PSD scenarios, which are similar to the grain size  
481 distribution of beach sand, resulted in a maximum transport reduction of 15% over one day and 7.5%  
482 over one year compared to the median grain size. These values are in a similar order of magnitude as  
483 those found by Hoonhout & de Vries (2016), although the presence of shells further exacerbated the  
484 resulting reduction in their study. The results indicate that for most scenarios, the median grain size can  
485 be used as a pragmatic metric for natural grain size distributions in aeolian sediment transport models  
486 at daily to yearly time scales.

487 However, there are some limitations to simplifying grain size distributions with the median grain size. In  
488 some of the single-fraction simulations, larger transport rates were recorded than in the corresponding  
489 multi-fraction simulation. Wide PSDs might include a relatively large contribution of both coarse and fine  
490 fractions. The fine fraction abundance may result in a relative increase of total transport compared to  
491 narrower PSDs (e.g., PSD 6 compared to PSD 4 and 5 in Figure 10). Additionally, several multi-fraction  
492 cases showed that increased transport can occur despite an increase in the reference grain size (e.g., the  
493 125/2000  $\mu\text{m}$  mix in Figure 7). This sediment transport increase is related to an increase in the bed  
494 roughness and the shear velocity (Equation 3). In all cases, the effect was temporary, as coarsening due  
495 to the removal of fines counteracted the increase in transport caused by the roughness.

496 The suitability of the  $D_{50}$  as a representative grain size can also be affected by armoring that limits the  
497 aeolian sediment transport. These armoring effects occur when a considerable amount of coarse grains  
498 is present. Whether specific grain sizes will result in armoring depends on the local wind climate. During  
499 energetic wind events, wind peaks can cause an increase in sediment transport and mobilization of  
500 coarse grains from the bed surface, which can expose underlying sediment (e.g., the 125/2000  $\mu\text{m}$  mix  
501 in Figure 7). For the synthetic wind climate that was generated and used in this study, about 2000  $\mu\text{m}$   
502 was a critical grain size. Future work could further quantify for which wind climates and grain size  
503 distributions the use of the  $D_{50}$  as a representative grain size is valid. For now, a representative wind  
504 forcing could be created based on the wind climate and used in an aeolian sediment transport model to  
505 determine to what extent specific coarse fractions are expected to be mobilized.

506 Besides wind speed peaks, hydrodynamic processes and trampling can also break up and alter armor  
507 layers. Hydrodynamic processes can cause erosion, deposition and mixing that directly affect the top  
508 layers of the bed surface on a time scale of seasons (e.g., Abuodha, 2003; Prodger et al., 2017), events  
509 (e.g., Gallagher et al., 2016) and tides (e.g., van IJendoorn et al., 2022). Future work could investigate  
510 the effect of temporally varying grain sizes due to hydrodynamic processes on the sediment flux by

511 including temporal grain size variations in modeling simulations by making simplified assumptions (e.g.  
512 based on findings by van IJendoorn et al., 2022) or coupling with a numerical model (Reniers et al.,  
513 2013; Srisuwan & Work, 2015). Trampling is also expected to affect the grain size at the bed surface  
514 (Moayeri et al., 2023; Reyes-Martínez et al., 2015). Its effects could be included in aeolian sediment  
515 transport models with mixing of surface layers in locations where human activity is expected.

## 516 **5.2. The implementation of spatial grain size variations in aeolian sediment transport modeling**

517 Significant vertical grain size variations at the bed surface have been measured (e.g., van IJendoorn et  
518 al., 2022) and over larger soil depths (e.g., Gallagher et al., 2016; Gunaratna et al., 2019). The  
519 measurements of van IJendoorn et al. (2022) showed a maximum range of 119  $\mu\text{m}$  in the  $D_{50}$  of  
520 different layers in the top 5 cm of the bed surface. Based on our results, we expect that these variations  
521 could be simulated relatively accurately on the daily and yearly timescales with the  $D_{50}$ . On the minute-  
522 scale, we expect that the sediment flux could significantly be altered, especially when layers with a  
523 significant contribution of coarse fraction are present near the bed surface. We recommend the  
524 inclusion of vertical grain size layering in aeolian sediment transport models where short-term time  
525 scales are considered. On time scales longer than days, they can be omitted.

526 The source area at the beginning of the domain has a significant impact on the cumulative sediment flux  
527 across all time scales. As a result, there can be a disconnect between the grain size that is at the bed  
528 surface and the transport that occurs at that location. Consider a point measurement at the end of the  
529 domain of the coarse - fine and fine - coarse - fine cases for the 10-minute time scale (Figure 13). The  
530 grain size at these locations was comparable but the cumulative sediment flux deviated considerably.  
531 This difference was mostly related to the grain size of the material present in the source area where  
532 pickup of fine and coarse sediment occurred. This shows it is important to consider the grain size that is  
533 present in the source area when explaining minute-scale sediment transport measurements, as  
534 previously indicated by Cohn et al., (2022), Field and Pelletier (2018) and Uphues et al. (2021). These  
535 grain size measurements should be recent because wind speed peaks can cause temporal variations in  
536 the bed surface grain size and the related aeolian sediment transport.

537 The intertidal area was found to be an important source for aeolian sediment transport towards the  
538 dunes by de Vries, (2014a). Our findings show that this upwind source of sediment is important for the  
539 bed surface grain size development across the domain and the sediment transport magnitude. Thus, the  
540 results suggest that the grain size in the intertidal area (e.g., Bascom, 1951) might be the most

541 important to include in aeolian sediment transport models that are used for coastal dune development  
542 predictions. These findings align with measurements of aeolian sediment transport in the intertidal area  
543 by Swann et al., (2021), who found similar grain sizes in the air column as on the bed. Future work could  
544 further validate or falsify these findings by combining minute-scale quantitative sediment transport  
545 measurements with bed surface grain size measurements that can show a temporal variation through  
546 time. Furthermore, the importance of the grain size in the intertidal area emphasizes the need to study  
547 sediment supply by hydrodynamic processes and, specifically, its effect on grain size composition.

## 548 **6. Conclusions**

549 The sorting of multi-fraction sediment, spatial variations in grain size, and their impact on aeolian  
550 sediment transport were studied using a numerical aeolian sediment transport model. Results show  
551 that, in general, the  $D_{50}$  can be used as a representative grain size in aeolian sediment transport  
552 modeling on a time scale of days to years. For wide grain size distributions, the multi-fraction sediment  
553 flux may differ from the single-fraction flux of the reference grain size. In these cases, simplified model  
554 runs that include the full particle size distribution and a wind forcing representative for the wind climate  
555 to test the impact on the sediment flux could be considered.

556 On a time scale of 10-minutes, the bed surface grain size has a direct effect on the aeolian sediment  
557 transport flux. Due to this strong relation between grain size and sediment transport, vertical grain size  
558 layering may be required in models that predict aeolian sediment transport at this time scale. On time  
559 scales from days to years, modeling the effect of vertical layering may not be needed if a representative  
560 grain size is used.

561 The effect of horizontal grain size variations is relevant across all time scales. The grain size in the  
562 upwind part of the domain can directly affect the transport magnitude across the domain. The intertidal  
563 area can be the dominant source of aeolian sediment transport that affects coastal dune development.  
564 In these cases, we recommend to include the grain size present in this region in aeolian sediment  
565 transport models and consider its impact on point measurements of sediment transport recorded on the  
566 beach. Additionally, we recommend to further investigate the supply of sediment to the intertidal zone  
567 by marine processes, specifically focusing on grain size.

## 568 **Acknowledgments**

569 This work is part of the research program DuneForce with project number 17064, which is (partly)  
570 financed by the Dutch Research Council (NWO)

571 **Data availability statement**

572 Version 2.1.0 of the AeoliS software used for the aeolian sediment transport simulations in this research  
573 is preserved at <https://doi.org/10.4121/22215562>, available via GPL-3.0 and developed openly on  
574 Github (<https://github.com/openeearth/aeolis-python>). The Python code used for the analysis and figure  
575 generation is hosted at Github (<https://github.com/christavaniizendoorn/grainsizeanalysis-aeolis>) and is  
576 preserved at <https://doi.org/10.4121/22220134>, version 1.1.0, under GPL-3.0.

577 **References**

578 Abuodha, J. O. Z. (2003). Grain size distribution and composition of modern dune and beach sediments,  
579 Malindi Bay coast, Kenya. *Journal of African Earth Sciences*, 36(1–2), 41–54.

580 [https://doi.org/10.1016/S0899-5362\(03\)00016-2](https://doi.org/10.1016/S0899-5362(03)00016-2)

581 AeoliS Development Team. (2023). *AeoliS (Version v2.1.0)*. [Software]. 4TU Repository.

582 <https://doi.org/10.4121/22215562>

583 Anderson, R. S., & Haff, P. K. (1988). Simulation of Eolian Saltation. *Science*, 241(4867), 820–823.

584 <https://doi.org/10.1126/SCIENCE.241.4867.820>

585 Bagnold, R. A. (1937a). The size-grading of sand by wind. *Proceedings of the Royal Society of London*.  
586 *Series A - Mathematical and Physical Sciences*, 163(913), 250–264.

587 <https://doi.org/10.1098/rspa.1937.0225>

588 Bagnold, R. A. (1937b). The Transport of Sand by Wind. *The Geographical Journal*, 89(5), 409.

589 <https://doi.org/10.2307/1786411>

590 Bascom, W. N. (1951). The relationship between sand size and beach-face slope. *Eos, Transactions*  
591 *American Geophysical Union*, 32(6), 866–874. <https://doi.org/10.1029/TR032I006P00866>

592 Bauer, B. O. (1991). Aeolian Decoupling of Beach Sediments. *Annals of the Association of American*  
593 *Geographers*, 81(2), 290–303. <https://doi.org/10.1111/j.1467-8306.1991.tb01691.x>

594 Bauer, B. O., & Davidson-Arnott, R. G. D. (2002). A general framework for modeling sediment supply to  
595 coastal dunes including wind angle, beach geometry, and fetch effects. *Geomorphology*, 49(1–2),  
596 89–108. [https://doi.org/10.1016/S0169-555X\(02\)00165-4](https://doi.org/10.1016/S0169-555X(02)00165-4)

597 Bristow, N. R., Best, J., Wiggs, G. F. S., Nield, J. M., Baddock, M. C., Delorme, P., & Christensen, K. T.

598 (2022). Topographic perturbation of turbulent boundary layers by low-angle, early-stage aeolian

599 dunes. *Earth Surface Processes and Landforms*, 47(6), 1439–1454.  
600 <https://doi.org/10.1002/ESP.5326>

601 Çelikoğlu, Y., Yüksel, Y., & Sedat Kabdaşlı, M. (2006). Cross-Shore Sorting on a Beach under Wave Action.  
602 *Journal of Coastal Research*, 22(3 (223)), 487–501. <https://doi.org/10.2112/05-0567.1>

603 Cheng, H., He, J., Zou, X., Li, J., Liu, C., Liu, B., ... Kang, L. (2015). Characteristics of particle size for  
604 creeping and saltating sand grains in aeolian transport. *Sedimentology*, 62(5), 1497–1511.  
605 <https://doi.org/10.1111/SED.12191>

606 Cohn, N., Dickhudt, P., & Marshall, J. (2022). In-situ measurement of grain size characteristics within the  
607 aeolian saltation layer on a coastal beach. *Earth Surface Processes and Landforms*, 47(9), 2230–  
608 2244. <https://doi.org/10.1002/ESP.5373>

609 de Vries, S., Arens, S. M., de Schipper, M. A., & Ranasinghe, R. (2014a). Aeolian sediment transport on a  
610 beach with a varying sediment supply. *Aeolian Research*.  
611 <https://doi.org/10.1016/j.aeolia.2014.08.001>

612 de Vries, S., van Thiel de Vries, J. S. M., van Rijn, L. C., Arens, S. M., & Ranasinghe, R. (2014b). Aeolian  
613 sediment transport in supply limited situations. *Aeolian Research*, 12, 75–85.  
614 <https://doi.org/10.1016/j.aeolia.2013.11.005>

615 Delgado-Fernandez, I. (2010). A review of the application of the fetch effect to modelling sand supply to  
616 coastal foredunes. *Aeolian Research*, 2(2–3), 61–70. <https://doi.org/10.1016/j.aeolia.2010.04.001>

617 Dong, Z., Wang, H., Liu, X., & Wang, X. (2004). A wind tunnel investigation of the influences of fetch  
618 length on the flux profile of a sand cloud blowing over a gravel surface. *Earth Surf. Process.*  
619 *Landforms*, 29, 1613–1626. <https://doi.org/10.1002/esp.1116>

620 Durán, O., Claudin, P., & Andreotti, B. (2011). On aeolian transport: Grain-scale interactions, dynamical  
621 mechanisms and scaling laws. *Aeolian Research*, 3(3), 243–270.  
622 <https://doi.org/10.1016/J.AEOLIA.2011.07.006>

623 Edwards, A. C. (2001). Grain size and sorting in modern beach sands. *Journal of Coastal Research*, 17(1).

624 Field, J. P., & Pelletier, J. D. (2018). Controls on the aerodynamic roughness length and the grain-size  
625 dependence of aeolian sediment transport. *Earth Surface Processes and Landforms*, 43(12), 2616–  
626 2626. <https://doi.org/10.1002/ESP.4420>

627 Gallagher, E. L., Wadman, H., McNinch, J., Reniers, A., & Koktas, M. (2016). A Conceptual Model for  
628 Spatial Grain Size Variability on the Surface of and within Beaches. *Journal of Marine Science and*  
629 *Engineering* 2016, Vol. 4, Page 38, 4(2), 38. <https://doi.org/10.3390/JMSE4020038>

630 Gao, X., Narteau, C., & Rozier, O. (2016). Controls on and effects of armoring and vertical sorting in  
631 aeolian dune fields: A numerical simulation study. *Geophysical Research Letters*, 43(6), 2614–2622.  
632 <https://doi.org/10.1002/2016GL068416>

633 Gillette, D. A., Herbert, G., Stockton, P. H., & Owen, P. R. (1996). Causes of the fetch effect in wind  
634 erosion. *Earth Surface Processes and Landforms*, 21, 641–659. [https://doi.org/10.1002/\(SICI\)1096-](https://doi.org/10.1002/(SICI)1096-9837(199607)21:7)  
635 [9837\(199607\)21:7](https://doi.org/10.1002/(SICI)1096-9837(199607)21:7)

636 Gunaratna, T., Suzuki, T., & Yanagishima, S. (2019). Cross-shore grain size and sorting patterns for the  
637 bed profile variation at a dissipative beach: Hasaki Coast, Japan. *Marine Geology*, 407, 111–120.  
638 <https://doi.org/10.1016/J.MARGEO.2018.10.008>

639 Hallin, C., Almström, B., Larson, M., & Hanson, H. (2019a). Longshore Transport Variability of Beach Face  
640 Grain Size: Implications for Dune Evolution. *Journal of Coastal Research*, 35(4), 751–764.  
641 <https://doi.org/10.2112/JCOASTRES-D-18-00153.1>

642 Hallin, C., Huisman, B. J. A., Larson, M., Walstra, D. J. R., & Hanson, H. (2019b). Impact of sediment  
643 supply on decadal-scale dune evolution — Analysis and modelling of the Kennemer dunes in the  
644 Netherlands. *Geomorphology*, 337, 94–110. <https://doi.org/10.1016/j.geomorph.2019.04.003>

645 Hallin, C., Larson, M., & Hanson, H. (2019c). Simulating beach and dune evolution at decadal to  
646 centennial scale under rising sea levels. *PLOS ONE*, 14(4), e0215651.  
647 <https://doi.org/10.1371/journal.pone.0215651>

648 Hoonhout, B., & de Vries, S. (2016). A process-based model for aeolian sediment transport and  
649 spatiotemporal varying sediment availability. *Journal of Geophysical Research: Earth Surface*,  
650 121(8), 1555–1575. <https://doi.org/10.1002/2015JF003692>

651 Hoonhout, B., & de Vries, S. (2019). Simulating spatiotemporal aeolian sediment supply at a mega  
652 nourishment. *Coastal Engineering*, 145, 21–35. <https://doi.org/10.1016/j.coastaleng.2018.12.007>

653 Houser, C. (2009). Synchronization of transport and supply in beach-dune interaction. *Progress in*  
654 *Physical Geography*, 33(6), 733–746. <https://doi.org/10.1177/0309133309350120>

655 Kroon, A., de Schipper, M., de Vries, S., & Aarninkhof, S. (2022). Subaqueous and Subaerial Beach  
656 Changes after Implementation of a Mega Nourishment in Front of a Sea Dike. *Journal of Marine*  
657 *Science and Engineering* 2022, Vol. 10, Page 1152, 10(8), 1152.  
658 <https://doi.org/10.3390/JMSE10081152>

659 Krumbein, W. C. (1934). Size frequency distributions of sediments. *Journal of Sedimentary Research*,  
660 4(2), 65–77. <https://doi.org/10.1306/D4268EB9-2B26-11D7-8648000102C1865D>

661 Liu, Y., Liu, X., & Sun, Y. (2021). QGrain: An open-source and easy-to-use software for the comprehensive  
662 analysis of grain size distributions. *Sedimentary Geology*, 423, 105980.  
663 <https://doi.org/10.1016/J.SEDGEO.2021.105980>

664 McKenna Neuman, C., & Bédard, O. (2017). A wind tunnel investigation of particle segregation, ripple  
665 formation and armouring within sand beds of systematically varied texture. *Earth Surface*  
666 *Processes and Landforms*, 42(5), 749–762. <https://doi.org/10.1002/ESP.4019>

667 McKenna Neuman, C., Li, B., & Nash, D. (2012). Micro-topographic analysis of shell pavements formed  
668 by aeolian transport in a wind tunnel simulation. *Journal of Geophysical Research: Earth Surface*,  
669 117(F4), 4003. <https://doi.org/10.1029/2012JF002381>

670 Moayeri, V., Miri, A., Shahriari, A., Rahdari, V., & Gill, T. E. (2023). A field study of the surface  
671 disturbance effects of animals and motor vehicles on aeolian sediment emission from a silty playa  
672 surface. *Environmental Research*, 216, 114606. <https://doi.org/10.1016/J.ENVRES.2022.114606>

673 Owen, P. R. (1964). Saltation of uniform grains in air. *Journal of Fluid Mechanics*, 20(2), 225–242.  
674 <https://doi.org/10.1017/S0022112064001173>

675 Prodger, S., Russell, P., & Davidson, M. (2017). Grain-size distributions on high-energy sandy beaches  
676 and their relation to wave dissipation. *Sedimentology*, 64(5), 1289–1302.  
677 <https://doi.org/10.1111/sed.12353>

678 Reniers, A. J. H. M., Gallagher, E. L., MacMahan, J. H., Brown, J. A., van Rooijen, A. A., van Thiel de Vries,  
679 J. S. M., & van Prooijen, B. C. (2013). Observations and modeling of steep-beach grain-size  
680 variability. *Journal of Geophysical Research: Oceans*, 118(2), 577–591.  
681 <https://doi.org/10.1029/2012JC008073>

682 Reyes-Martínez, M. J., Ruíz-Delgado, M. C., Sánchez-Moyano, J. E., & García-García, F. J. (2015).

683 Response of intertidal sandy-beach macrofauna to human trampling: An urban vs. natural beach  
684 system approach. *Marine Environmental Research*, 103, 36–45.  
685 <https://doi.org/10.1016/J.MARENRES.2014.11.005>

686 Sarre, R. D. (1987). Aeolian sand transport. *Progress in Physical Geography*, 11(2), 157–182.  
687 [https://doi.org/10.1177/030913338701100201/ASSET/030913338701100201.FP.PNG\\_V03](https://doi.org/10.1177/030913338701100201/ASSET/030913338701100201.FP.PNG_V03)

688 Sherman, D. J. (1992). An equilibrium relationship for shear velocity and apparent roughness length in  
689 aeolian saltation. *Geomorphology*, 5, 419–431.

690 Sonu, C. J. (1972). Bimodal Composition and Cyclic Characteristics of Beach Sediment in Continuously  
691 Changing Profiles. *SEPM Journal of Sedimentary Research*, 42(4), 852–857.  
692 <https://doi.org/10.1306/74d72653-2b21-11d7-8648000102c1865d>

693 Srisuwan, C., & Work, P. A. (2015). Beach Profile Model with Size-Selective Sediment Transport. II:  
694 Numerical Modeling. *Journal of Waterway, Port, Coastal, and Ocean Engineering*, 141(2),  
695 04014033. [https://doi.org/10.1061/\(ASCE\)WW.1943-5460.0000274](https://doi.org/10.1061/(ASCE)WW.1943-5460.0000274)

696 Stauble, D. K., & Cialone, M. A. (1997). Sediment Dynamics and Profile Interactions: DUCK94.  
697 *Proceedings of the Coastal Engineering Conference*, 4, 3921–3934.  
698 <https://doi.org/10.1061/9780784402429.303>

699 Swann, C., Lee, D., Trimble, S., & Key, C. (2021). Aeolian sand transport over a wet, sandy beach. *Aeolian*  
700 *Research*, 51, 100712. <https://doi.org/10.1016/J.AEOLIA.2021.100712>

701 van der Wal, D. (2000a). Grain-size-selective aeolian sand transport on a nourished beach. *Journal of*  
702 *Coastal Research*, 16(3).

703 van der Wal, D. (2000b). Modelling aeolian sand transport and morphological development in two beach  
704 nourishment areas. *Earth Surface Processes and Landforms*, 25(1), 77–92.  
705 [https://doi.org/10.1002/\(SICI\)1096-9837\(200001\)25:1<77::AID-ESP49>3.0.CO;2-M](https://doi.org/10.1002/(SICI)1096-9837(200001)25:1<77::AID-ESP49>3.0.CO;2-M)

706 van IJzendoorn, C. O. (2023). *Python code for the analysis of AeoliS grain size scenarios (Version 1.1.0)*  
707 *[Software]*. 4TU Repository. <https://doi.org/10.4121/22220134>

708 van IJzendoorn, C. O., Hallin, C., Cohn, N., Reniers, A. J. H. M., & de Vries, S. (2022). Novel sediment  
709 sampling method provides new insights into vertical grain size variability due to marine and aeolian  
710 beach processes. *Earth Surface Processes and Landforms*. <https://doi.org/10.1002/ESP.5518>

711 van Rijn, L. C., & Strypsteen, G. (2020). A fully predictive model for aeolian sand transport. *Coastal*  
712 *Engineering*, 156, 103600. <https://doi.org/10.1016/J.COASTALENG.2019.103600>

713 Zhang, P., Sherman, D. J., & Li, B. (2021). Aeolian creep transport: A review. *Aeolian Research*, 51,  
714 100711. <https://doi.org/10.1016/J.AEOLIA.2021.100711>

715